

Microstructure and Sliding Wear Behavior of Fe-Based Coatings Manufactured with HVOF and HVAF Thermal Spray Processes

A. Milanti, V. Matikainen, G. Bolelli, H. Koivuluoto, L. Lusvarghi, and P. Vuoristo

(Submitted September 25, 2015; in revised form February 10, 2016)

The microstructure and micromechanical behavior of thermally sprayed Fe-based coatings manufactured with high-velocity oxygen fuel (HVOF) and high-velocity air fuel (HVAF) processes were investigated. Fe-Cr-Ni-Si-B-C and Fe-Cr-Ni-Mo-Si-B-C powders were used as the feedstock materials. The coatings showed a highly dense microstructure with near-zero oxidation. The microstructure of the feedstock powders was better retained when sprayed with HVAF process. Differential scanning calorimetry revealed two small exothermic peaks at about 600 °C for the HVOF-sprayed coatings, without any increase in weight in thermogravimetric analysis. It suggested the re-precipitation of carbides that were dissolved during spraying due to the higher particle temperature reported by spray diagnostics system during the HVOF process (≈ 1800 °C) compared to the HVAF one (≈ 1400 °C). Micro- and nano-indentations helped to show the difference in inter-lamellar cohesive strength and, in turn, in the particle deposition mechanism. Coatings sprayed with Fe-Cr-Ni-Mo-Si-B-C composition possessed higher sliding wear resistance than that of Fe-Cr-Ni-Si-B-C due to higher nano-hardness. More specifically, HVOF-sprayed Fe-Cr-Ni-Mo-Si-B-C coating showed the largest intra-lamellar hardness, the largest elasticity, and high quality of particle interfaces which resulted in lower sliding wear rate.

Keywords iron alloys, protective coatings, wear resistant coatings

1. Introduction

Global economic crisis together with more strict environmental restrictions on materials and industrial manufacturing processes have been forcing the research community to find cheaper and environmentally friendly solutions to increase the properties of bulk materials employed in several industrial applications such as mechanical equipment manufacturing, hydraulic components, pulp and paper manufacturing, aerospace technologies, electrical engineering, and off-shore structures. Among several approaches, surface engineering is widely acknowledged as the main viable way to increase mechanical and chemical properties of bulk materials at affordable costs by modification of surfaces when wear, corrosion, fatigue, or creep are involved (Ref 1). Modification of the surfaces can be attained without alteration of the chemistry (e.g., thermal or mechanical treatments), with the alteration of the chemistry (e.g., thermochemical

diffusion, chemical treatments) or by adding layers of material (Ref 2). Thermal spray technology belongs to the last category and it is gaining more and more attention due to the high versatility and the relatively low cost. A thermal spray process consists of a feedstock material (powders, wires, or rods), a source of heat, a spray gun, and a jet of gases which accelerate particles towards a substrate, onto which they impact to build a coating (Ref 3). For wear and corrosion applications, Ni-, Co-based alloys and hardmetals have been extensively deposited by thermal spray processes because of their good mechanical and chemical properties (Ref 4-7). However, over the last 10 years the price of Ni- and Co-based alloys remarkably grew (up to 40×10^3 euro/ton and now at about 10×10^3 euro/ton) forcing the main producers to overcome the problem by finding alternative suitable solutions (Ref 8).

Moreover, the International Agency for Research on Cancer recognized six metals and/or their compounds as human carcinogens (arsenic, beryllium, cadmium, hexavalent chromium, cobalt, and nickel). Even though the mechanisms of action of carcinogenic metals such as Co and Ni are still far from being completely elucidated, several regulations limit the usage of Ni and Co and their compounds due to the potential risk (e.g., toxicity, carcinogenicity, and dermal sensitization) in certain circumstances (Ref 9-12). Hériaud-Kraemer and Montavon (Ref 13) also highlighted the potential and real risks that workers are exposed to in thermal spray industry. Cobalt and nickel were found to possess one of the lowest permissible exposure limit (PEL) and short-term exposure limit (STEL) values that the workers can be exposed to

A. Milanti, V. Matikainen, H. Koivuluoto, and P. Vuoristo, Department of Materials Science, Tampere University of Technology, Tampere, Finland; and G. Bolelli and L. Lusvarghi, Department of Engineering “Enzo Ferrari”, University of Modena and Reggio Emilia, Modena, Italy. Contact e-mail: andrea.milanti@tut.fi.

among several metallic materials studied (only hexavalent chromium and lead were reported to be more harmful).

In such a scenario, Fe-based alloys have gained growing interest over the last years in the material engineering community due to their low and stable price, high corrosion resistance, high mechanical properties, coupled to the absence of environmental restrictions and to their easy machinability (Ref 13, 14). For such reasons, over the last 50 years Fe-based powders have been extensively sprayed with conventional thermal spray processes such as arc spraying (AS), flame spraying (FS), atmospheric plasma spraying (APS), and recently with high-velocity oxygen fuel spraying (HVOF) and high-velocity air fuel spraying (HVOF). APS, AS, and FS are characterized by high particle temperature and low particle velocity which, in the absence of a proper shrouding atmosphere, result in extensive interaction of molten particles with air and in non-uniform heating and solidification. This leads to low hardness and to high oxide and porosity content up to 10%, which, in turn, barely offer good protection against aggressive solutions penetrating towards the substrate (Ref 15-20). Oxidation and phase transformations of APS-sprayed Fe-based coatings were reported by Morks et al. (Ref 15) by studying the chemical composition and the splat morphology. In Ref 16, the oxidation behavior of two high-alloyed steel powders sprayed by water-stabilized plasma gun was investigated. Non-stoichiometric mixed Fe- and Cr-rich FeCr_2O_4 oxides were also reported to occur during the in-flight stage (Ref 16). Microcracks, high porosity, and fairly low micro-hardness were shown in FS-sprayed Fe-based coatings by Redjda et al. in Ref 18 as well as by Wielage et al. in Ref 19 in Fe-based coatings manufactured by AS process.

Conversely, Fe-based coatings were reported to possess promising characteristics when manufactured with high kinetic thermal spray processes such as high-velocity oxygen fuel (HVOF) and high-velocity air fuel (HVOF) (Ref 21-25). HVOF and HVOF spray processes are based on supersonic jets achieved by the expansion of the products of combustion between oxygen (HVOF) or air (HVOF) and a fuel (hydrogen or hydrocarbons) through a convergent-divergent nozzle. The feedstock material is fed as powder, which is heated and accelerated by the high-velocity gas stream. HVOF and HVOF processes were reported to produce dense metallic coatings with an excellent adhesion to the substrate and without extensive thermal deterioration of the sprayed material (Ref 21-25). Furthermore, the high deposition rate and efficiency (Ref 3) and the lower spray temperature make such processes solid and reliable solutions to spray dense and oxide-free Fe-based coatings fulfilling the industrial requirements (e.g., high hardness, near-zero oxide content, low porosity) (Ref 21-25).

However, the HVOF process significantly differs from the HVOF one by providing lower flame temperature and higher gas velocity due to the complete replacement of oxygen with air and by the different architecture of the torch. In-flight particle temperatures in different generations of HVOF torches range from 1500 °C up to 2100 °C whereas, in HVOF torches, they range from 1000 °C up to

1500 °C (Ref 3). With regard to in-flight particle velocity, in the HVOF process particles acquire much higher velocity, up to 1000 m/s, when compared to values of ≈ 700 m/s for HVOF (Ref 26, 27). The choice of HVOF over HVOF may, therefore, modify key coating properties such as the oxide content, porosity and inter-particle cohesion, phase composition, and residual stresses. For instance, Guo et al. (Ref 22) have highlighted the possibility to diminish the oxide content using HVOF, which in turn resulted in higher corrosion resistance because of the presence of fewer diffusion paths for electrolyte to penetrate towards the substrate. In addition, the HVOF process was reported to retain better powder microstructure, avoiding any harmful reaction at high temperature (Ref 22, 23).

The present paper focuses on the microstructural and micromechanical differences between two Fe-based materials, Fe-Cr-Ni-Si-B-C and Fe-Cr-Ni-Mo-Si-B-C, sprayed with HVOF and HVOF processes, and their combined effect on sliding wear behavior. This study aims to achieve a better understanding of HVOF and HVOF spraying processes when dealing with Fe-based powders, helping to validate these coatings as further alternative solutions when anti-wear properties are needed.

2. Experimental Procedure

2.1 Materials and Manufacturing

Two gas-atomized Fe-based powders with nominal particle size distribution of $-40 + 20 \mu\text{m}$, with chemical composition Fe-31Cr-12Ni-3.6B-0.6C (wt.%) (Durum Verschleiss-Schutz GmbH, Krefeld, Germany) and Fe-31Cr-12Ni-2Mo-3.6B-0.6C (wt.%) (Wall Colmonoy Ltd., Pontardawe, UK), hereafter called Fe and Fe(Mo), respectively, were employed as the feedstock. More details of the powders are presented in our previous studies (Ref 28, 29). Spherical particle shape with smooth surface and low amount of satellites allowed good flowability in thermal spray feeding systems.

The powders were sprayed onto low carbon steel (Fe52) plates ($15 \times 5 \times 0.5 \text{ cm}$) by Diamond Jet Hybrid 2700 (DJH-2700, Oerlikon Metco, Wohlen, Switzerland) HVOF gun and M3 (Unicoat Technologies LLC, Oilville, USA) HVOF gun. Propane was used as the main combustion fuel gas for both thermal spray deposition processes. The process parameters for the deposition of the Fe-based coatings are presented in Table 1. The average particle temperatures were measured with Spraywatch 4s camera (Oseir Ltd., Tampere, Finland). The measurement is based on two-color pyrometry technique and was carried out at the spray distance.

2.2 Microstructural and Mechanical Characterization of Powders

The microstructure of the powders was further investigated in the present paper by observing the cross section with a field-emission scanning electron microscope (FES-

Table 1 HVOF DJH-2700 and HVAF M3 spraying process parameters

	HVOF (DJH2700)		HVAF (M3)	
Powder	Fe	Fe(Mo)	Fe	Fe(Mo)
Sample name	HVOF Fe	HVOF Fe(Mo)	HVAF Fe	HVAF Fe(Mo)
Air	375 slpm	375 slpm	0.80 MPa	0.80 MPa
Propane gas 1	70 slpm	70 slpm	0.73 MPa	0.73 MPa
Propane gas 2	/	/	0.76 MPa	0.76 MPa
Oxygen	240 slpm	240 slpm	/	/
Nitrogen carrier gas, L/min	12.5	12.5	60	60
Powder feeding rate, g/min	60	60	75	75
Stand-off distance, mm	230	230	300	300
Step size, mm	4.5	4.5	4	4
Thickness per pass, μm	16.2 ± 0.6	12.4 ± 0.3	84.7 ± 1.9	99.7 ± 1.7

EM, Zeiss ULTRAplus) equipped with EDX microanalysis (INCA, Oxford instruments, High Wycombe, UK). EDX element linescan, which consisted in collecting characteristic x-ray emissions of Fe, Cr, Ni, and Mo along a line of few micrometer length comprising some relevant microstructural details, was performed for 600 s on a sequence of precipitations (line length $\approx 5 \mu\text{m}$). X-ray diffractometry (XRD: Empyrean, PANalytical, The Netherlands, Co-K α radiation) was employed to assess phase composition. Experimental conditions include 2θ range 20° - 120° , step size 0.02° , beam mask 20 mm, programmable divergent slit fixed at $1/2$ degree, Fe-filter, and PANalytical PIXcel 3D detector. Phase identification was performed using the PANalytical X'Pert High Score Plus software using the ICDD JCPDF-2 database (International Centre for Diffraction Data, Newtown Square, PA, USA). A rotational stage was used for the powders to reduce the preferred orientation effect. The thermal behavior of the powders was assessed by simultaneous differential scanning calorimetry and thermogravimetry (DSC-TG: DTA 404, Netzsch, Selb, Germany) performed in air using Al_2O_3 crucibles with heating rate of $20^\circ\text{C}/\text{min}$, from room temperature up to $1400^\circ\text{C}/\text{min}$. Berkovich nano-indentation test was also performed on the polished cross sections of the powders, operating in load control mode (NHT, Anton-Paar TriTec, Peseux, Switzerland: 10 mN max. load, 15 mN/min loading/unloading rate, 15 s holding time at maximum load).

2.3 Microstructural and Mechanical Characterization of Coatings

Microstructural investigation of the sprayed coatings was carried out by FESEM, equipped with EDX microanalysis. Element linescan (same setup used for the powders) was also performed on coating cross sections. Phase composition was assessed by XRD, under the same experimental conditions as described in section 2.2 but using a fixed sample-holder platform instead of the rotational stage. Thermal behavior of the coatings was also investigated by simultaneous differential scanning calorimetry and thermogravimetry (DSC-TG) using the same experimental setup employed for the powders. Prior to testing, the coatings were manually milled using an

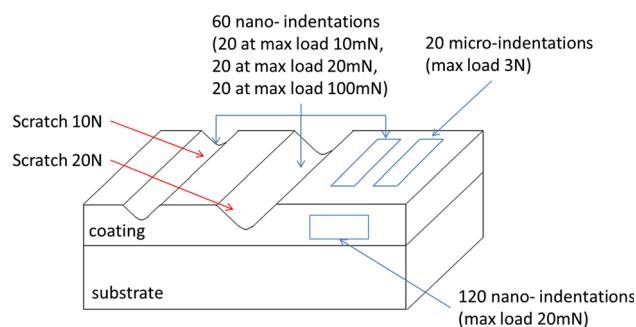


Fig. 1 Schematic representation of set of indentations performed on the studied coatings

agate mortar to minimize sample contamination. Comparison of thermal behavior between the powders and the coatings sprayed with HVOF and HVAF processes allowed us to obtain preliminary information on the effect of the spraying process on the microstructure.

Depth-sensing Berkovich micro-indentation (Micro-Combi tester, Anton-Paar TriTec) and nano-indentation (NHT, Anton-Paar TriTec) tests were also performed in order to evaluate the inter-lamellar and intra-lamellar hardness (intrinsic hardness of sprayed particles), respectively (Fig. 1). Nano-indentations on polished cross sections were purposely placed avoiding any particle boundaries in order to assess the intra-lamellar hardness. Micro-indentations on polished surfaces were performed with maximum load of 3 N, loading/unloading rate of 4.5 N/min, and holding time at maximum load of 15 s. Nano-hardness was averaged over 120 nano-indentations performed on coating cross section under load control (20 mN normal load, loading/unloading rate 35 mN/min, holding time 15 s). Nano- and Micro-Vickers hardness was calculated through the Oliver-Pharr procedure (Ref 30) in accordance with the ISO 14577 standards (Ref 31).

Coating surface elasticity was estimated by the parameter $\eta_{IT} = W_{el}/W_{tot}$ defined as the ratio of the elastic work of the indentation (computed as the area under the unloading part of the load-penetration curve) and the total work of the indentation (area under the loading part of the curve) through the micro-indentations while the elasticity

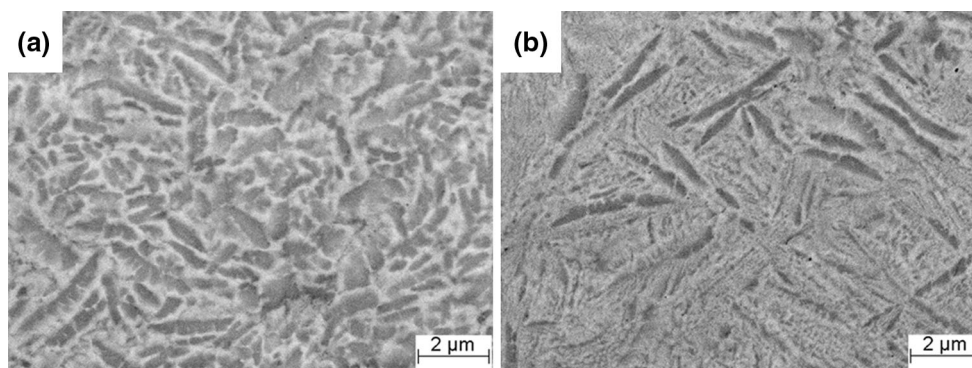


Fig. 2 Cross-sectional structure of Fe (a) and Fe(Mo) (b) powders (FESEM images)

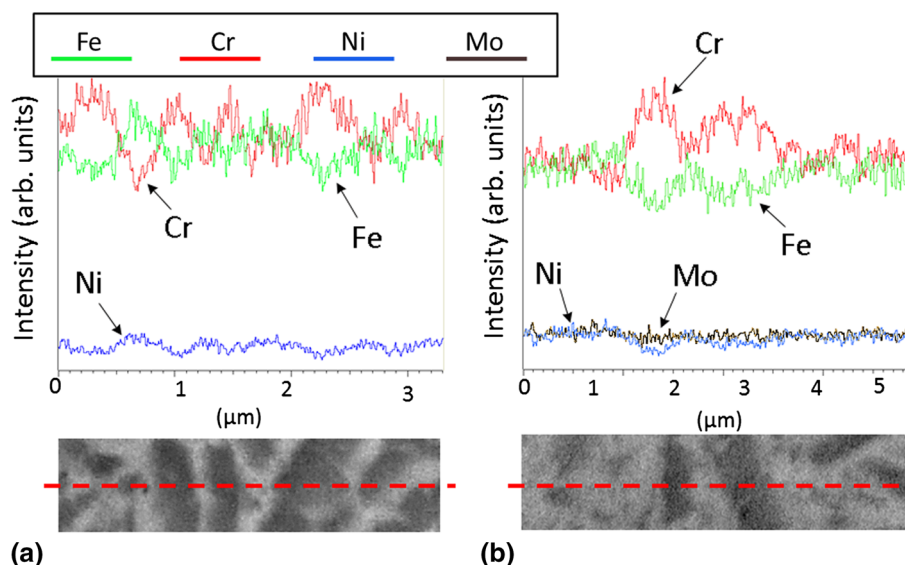


Fig. 3 EDX linescan microanalysis on the corresponding FESEM investigated area of powders. Fe, Cr, Ni, and Mo represented in Fe (a) and Fe(Mo) (b) powders

of a single splat (intra-lamellar surface elasticity) was also calculated from nano-indentation results.

Scratch test (Micro-Combi Tester, Anton-Paar TriTec) was also carried out on the polished surfaces of the coatings. A Rockwell C-type conical diamond indenter with rounded tip (200 μm radius) was chosen for the test. Linear scratch tests (1 unidirectional scratch pass) carried out at the constant load were performed. Two loads were employed (10 and 20 N), and in all cases the scratch length was 6 mm and scratch speed was 1 mm/min. The sole purpose of the scratch test was to investigate any possible work hardening on the grooves by nano-indentation. 60 nano-indentations at three different loads (100, 20, and 10 mN) were therefore performed at the bottom of the grooves after the scratch test. The same was done on the polished surfaces of the coatings to compare the results and to investigate whether or not material work hardening

occurred. The scheme of the entire mechanical indentation work is shown in Fig. 1.

As additional test in order to explain micromechanical differences found in HVAF-sprayed coatings, x-ray (Co-K α radiation) residual stress analysis, using the ω -tilt method (Ref 32), on samples polished up to mirror-like surface finish was carried out. Line focus configuration with beam mask 20 mm and programmable divergent slit fixed at 1/2 degree with the Euler cradle stage was used. 7 symmetric ψ tilt values were employed corresponding to $\sin^2\psi = 0; 0.1; 0.2; 0.3$, along three directions corresponding to $\phi = 0^\circ, \phi = 45^\circ, \text{ and } \phi = 90^\circ$. The (3 1 1) peak of austenite, located at $2\theta = 110.95^\circ$, was acquired by scanning a 2θ range of 7° , and the deformation in the $(h k l) = (3 1 1)$ direction was determined. The method used is analytically described in a previous publication (Ref 32).

2.4 Dry Sliding Wear Testing

The dry sliding wear resistance of the coatings was assessed by a pin-on-disk tribometer with ball-on-disk configuration. The sample was embedded in phenolic resin, polished up to mirror-like surface finish, and fixed in the middle of a still table. A spherical alumina monocrystalline ball of 6.35 mm in diameter (nominal hardness ≈ 22 GPa), mounted on a rotating pin holding arm, is pressed onto the sample surface with 5 N normal load. Tests were carried out at room temperature, wear track radius was 5 mm, arm revolution speed was 150 rpm, and the test lasted for 50,000 laps (linear speed 8 cm/s, linear distance ≈ 1500 m). Test parameters are based on dry sliding wear map in Ref 33. The friction coefficient was continuously measured throughout the test. The wear track was measured through optical profilometer (Alicona profilometer) in order to calculate the volume loss. The wear scars were also inspected by SEM equipped with EDX microanalysis (top view) and by FESEM (cross section) in order to give a better interpretation of wear mechanisms. Dry sliding wear rate (K) is calculated according to (Eq 1):

$$K[\text{mm}^3/(\text{Nm})] = V/(w \cdot s), \quad (\text{Eq } 1)$$

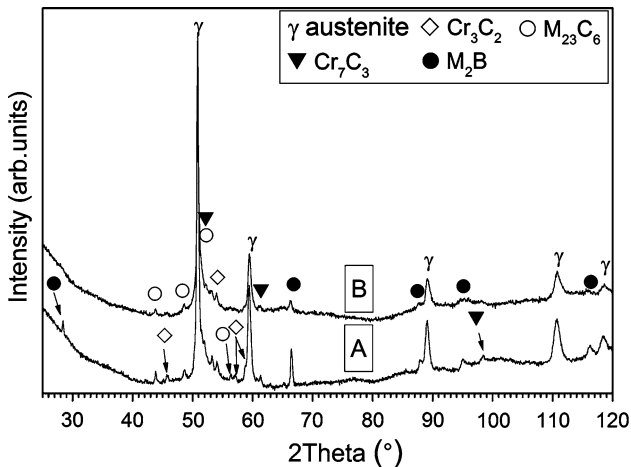


Fig. 4 XRD patterns of Fe (a) and Fe(Mo) (b) powders

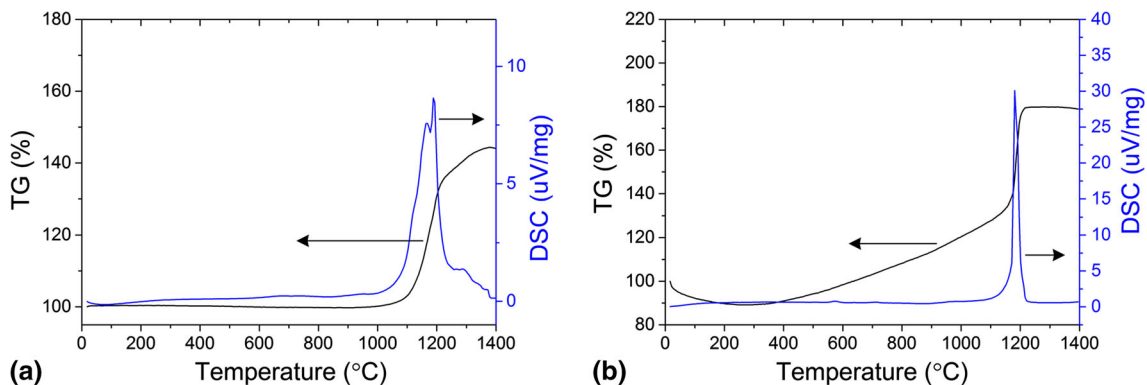


Fig. 5 DSC and TG analysis of the Fe (a) and Fe(Mo) (b) powders

where V is the volume loss (mm^3), w is the normal load (N), and s is the sliding distance (m).

Alumina counterpart wear track was observed through optical microscopy and wear rate was measured as well.

3. Results and Discussion

3.1 Microstructural Characteristics, Micromechanical Properties, and Thermal Behavior of Powders

Both powders were characterized by high content of long-shaped acicular dark precipitates (Fig. 2), enriched in Cr compared to the surrounding material enriched in Fe and Ni (Fig. 3: the high magnification EDX linescan shows the contents of Fe, Cr, Ni, and Mo evaluated through precipitates and surrounding area). In the Fe(Mo) powder, the content of Mo seems to be fairly constant throughout the line (Fig. 3b). Besides acicular darker precipitates, the Fe(Mo) powder also showed a high concentration of tiny, round-shaped precipitates (Fig. 2) which might affect the overall micromechanical properties of the powder.

XRD pattern evaluation (Fig. 4) confirmed Cr-rich secondary phases due to the presence of several low-intensity peaks associated to Cr and Fe mixed carbides and borides (Cr_3C_2 98-061-7482, Cr_7C_3 01-089-5902, $(\text{Cr,Fe})_{23}\text{C}_6$ JCPDS 01-078-1500, $(\text{Cr,Fe})_2\text{B}$ JCPDS 01-072-1073) embedded in an austenitic (f.c.c.) Fe-rich matrix (JCPDS 00-03-0397) for both powders. No crystalline phases with Mo were found in XRD phase evaluation, much likely due to the similar atomic radius of Cr and Mo, which makes it difficult to distinguish phases when partial substitution occurred.

The thermal behavior of the powders (Fig. 5) is characterized by a strong exothermic DSC peak centered in at ≈ 1150 °C, corresponding to a catastrophic oxidation as suggested by the sudden weight gain in TG, consistent with another study on similar powders (Ref 34). The Fe powder showed the onset of the peak at about 1000-1050 °C, compared to 1100 °C for the Fe(Mo) powder. This is much likely due to the slightly broader particle size distribution of the Fe powder (Ref 28, 29) which led to higher presence of finer particles with higher reactivity

with air during oxidation test. However, Fe(Mo) powder showed a slight increase of weight at $T > 400$ °C probably due to a slow but perceivable oxidation (phenomenon not present in the Fe powder). It is worth noticing the higher exothermic peak value of Fe(Mo) powder peak (≈ 30 $\mu\text{V}/\text{mg}$) compared to that of Fe powder (< 10 $\mu\text{V}/\text{mg}$) and the higher weight gain ($\approx 80\%$ weight increase for the Fe(Mo) powder, $\approx 60\%$ for the Fe powder), which proved the slightly higher reactivity of Fe(Mo) powders in air at high temperature.

High Vickers nano-hardness was assessed for both powders (Table 2). Specifically, slightly higher hardness and overall elasticity were found for the Fe(Mo) powder. The small and rounded precipitates (Fig. 2) may therefore play a specific strengthening role.

3.2 Thermal Behavior, Microstructural, and Micromechanical Properties of the Coatings

Both coating materials sprayed with HVOF (HVOF Fe, HVOF Fe(Mo)) and HVOF (HVOF Fe, HVOF Fe(Mo)) processes exhibited fairly dense and similar structure (Fig. 6a-d) consisting of well-flattened particles with only few small noticeable pores and barely visible particle boundaries.

Table 2 Vickers nano-hardness and η_{IT} calculated for Fe and Fe(Mo) powders. Indentation load 100 mN

	Vickers nano-hardness	η_{IT} , %
Fe	891 ± 228	37.0 ± 4.1
Fe(Mo)	918 ± 156	40.0 ± 5.5

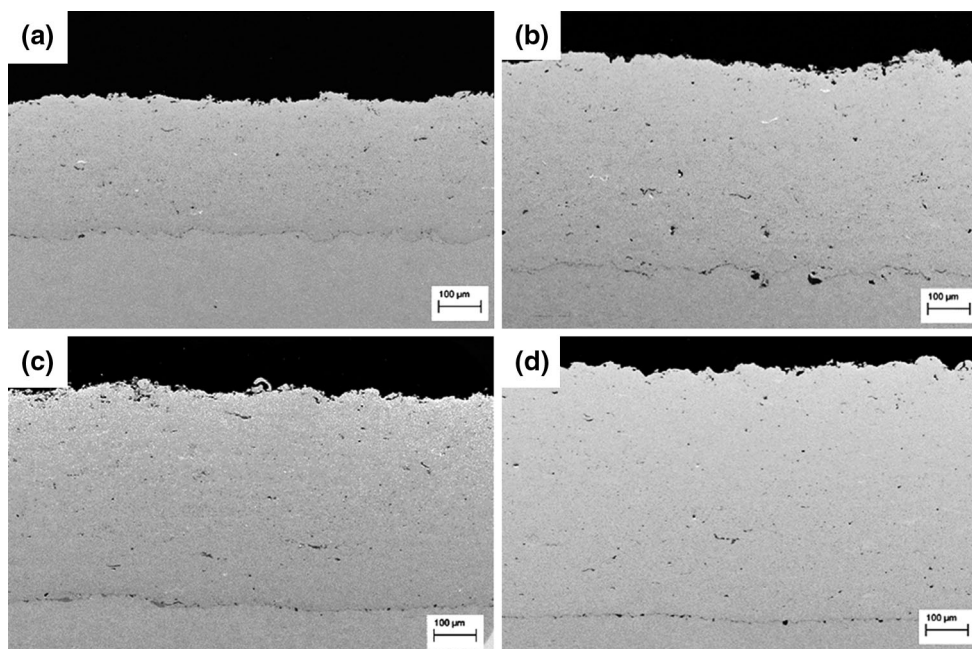


Fig. 6 Cross-sectional structure of HVOF Fe (a), HVOF Fe(Mo) (b), HVOF Fe (c), and HVOF Fe(Mo) (d) coatings. (FESEM images)

Detailed coating structures are presented in Fig. 7 in which limited oxidation is inferable by long dark oxide inter-lamellar stripes (Fig. 7b). Furthermore, the size and amount of dark and long-shaped secondary phases in the HVOF-sprayed coatings (Fig. 7c and d) are similar to those of feedstock powders proving a better preservation of powder microstructure in HVOF-sprayed coatings (HVOF Fe and HVOF Fe(Mo)) when compared to HVOF ones. Indeed, conversely to HVOF Fe and HVOF Fe(Mo), HVOF Fe and HVOF Fe(Mo) showed large precipitate-free areas (arrows in Fig. 7a and b). This difference is likely caused by the higher particle temperature measured at the spray distance: HVOF Fe = 1830 °C, HVOF Fe(Mo) = 1780 °C, HVOF Fe = 1430 °C, and HVOF Fe(Mo) = 1480 °C. More extensive melting of the HVOF-sprayed powders and, in particular, complete melting of the smallest particles result in high degree of secondary phase dissolution, with the formation of a metastable solid solution and possible vitrification during the impact and rapid cooling (Ref 22). Similar to the powders, Cr-rich precipitates embedded in a matrix enriched in Fe were confirmed by EDX linescan micro-analysis performed at high magnifications (Fig. 8). Element compositional peaks in EDX analysis of HVOF Fe and HVOF Fe(Mo) (Fig. 8a and b) seemed, however, more scattered than those of the corresponding powders (Fig. 3), suggesting the occurrence of some degree of secondary phase dissolution (Ref 34).

XRD patterns (Fig. 9) evaluation revealed the presence of austenitic (f.c.c.) γ matrix (JCPDS 00-03-0397) and few low-intensity peaks were associated with chromium and iron mixed carbides and borides (Cr_3C_2 —JCPDS 98-061-7482, Cr_7C_3 —JCPDS 01-089-5902, $(\text{Cr,Fe})_{23}\text{C}_6$ —JCPDS 01-078-1500, $(\text{Cr,Fe})_2\text{B}$ —JCPDS 01-072-1073).

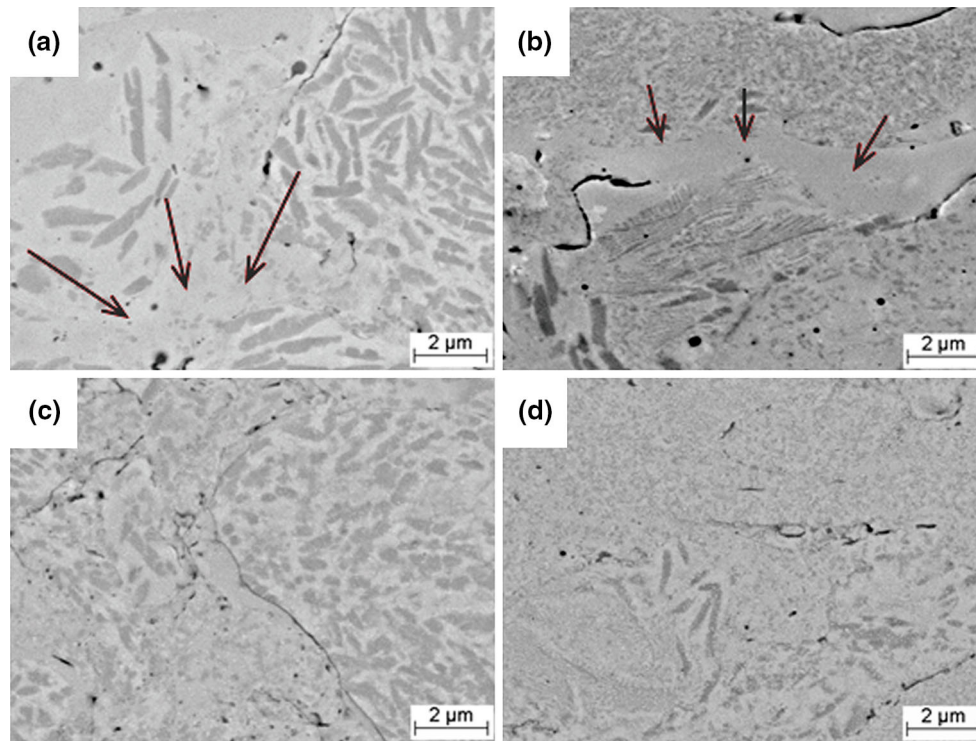


Fig. 7 High magnification of cross-sectional microstructure of HVOF Fe (a), HVOF Fe(Mo) (b), HVAF Fe (c), and HVAF Fe(Mo) (d) coatings. Red arrows pinpoint free-precipitate area (FESEM images)

However, most of the small peaks attributed to second phases (iron and chromium mixed carbides and borides) found in the XRD pattern of the powders (Fig. 4) seemed to disappear in the HVOF-sprayed coatings or to decrease in intensity in the HVAF ones. This might be caused by dissolution of carbides and borides during spraying as assumed in coating cross-sectional FESEM observation and EDX analysis, and/or to an increased amount of lattice defects due to severe plastic deformation upon impact of partially unmolten particles. In order to confirm partial secondary phase dissolution, the thermal behavior of the coatings was investigated from RT up to 1400 °C in air. The coatings were stripped off and finely ground for this purpose. All coatings showed the persistence of the strong exothermic peak at about 1200 °C in the DSC curve, accompanied by an increase of weight which suggests the occurrence of catastrophic oxidation (Fig. 10). When compared to the oxidation behavior of the powders (Fig. 5), the coatings displayed smaller DSC peaks and simultaneously lower weight change (≈ 10 versus ≈ 40 wt.% for the powders). This was much likely due to the lower surface exposed to reaction with air by the coating fragments during the test. The coatings sprayed with HVOF gun (HVOF Fe and HVOF Fe(Mo)) showed 2 small exothermic peaks (circles in Fig. 10) at about 600 °C. Such peaks were not detected for the powders. HVOF spraying partially dissolved the secondary phases present in the feedstock powders, forming much likely a metastable structure with dissolved carbides/borides.

During heating, re-precipitation of carbides and borides occurred at about 600 °C. Moreover, in the HVOF Fe(Mo), such exothermic peaks were slightly shifted towards higher temperatures compared to the HVOF Fe coating, proving the effect of the slightly different composition.

Conversely, such peaks are not detectable for HVAF-sprayed coatings (HVAF Fe and HVAF Fe(Mo)), proving that no dissolution occurred during spraying, so that no re-precipitation of carbides/borides takes place. The similarity in the thermal behavior of the powders and of the HVAF-sprayed coatings (HVAF Fe and HVAF Fe(Mo)) proved that the HVAF spraying process to be better for microstructure retention, compared to the HVOF spraying process. Further studies concerning the evaluation of the re-precipitated phases are needed in the future.

Furthermore, XRD patterns (Fig. 9) show the broadening of the most intense peak of the austenite (f.c.c.) γ matrix at $2\theta \approx 51^\circ$. In previous papers (Ref 28, 29), such broadening was attributed to grain refinement, to the accumulation of lattice defects, or to some extent of amorphous phase formation due to the high cooling rate after particle impact onto the substrate. Based on the previous DSC results, a low amount of amorphous phase might have been formed in the HVOF coatings, but not in the HVAF ones. Indeed, a small inflection without weight change occurs at about 700 °C for both HVOF-sprayed coatings (see the magnification of the DSC and TG curves of HVOF Fe and HVOF Fe(Mo) samples in Fig. 11),

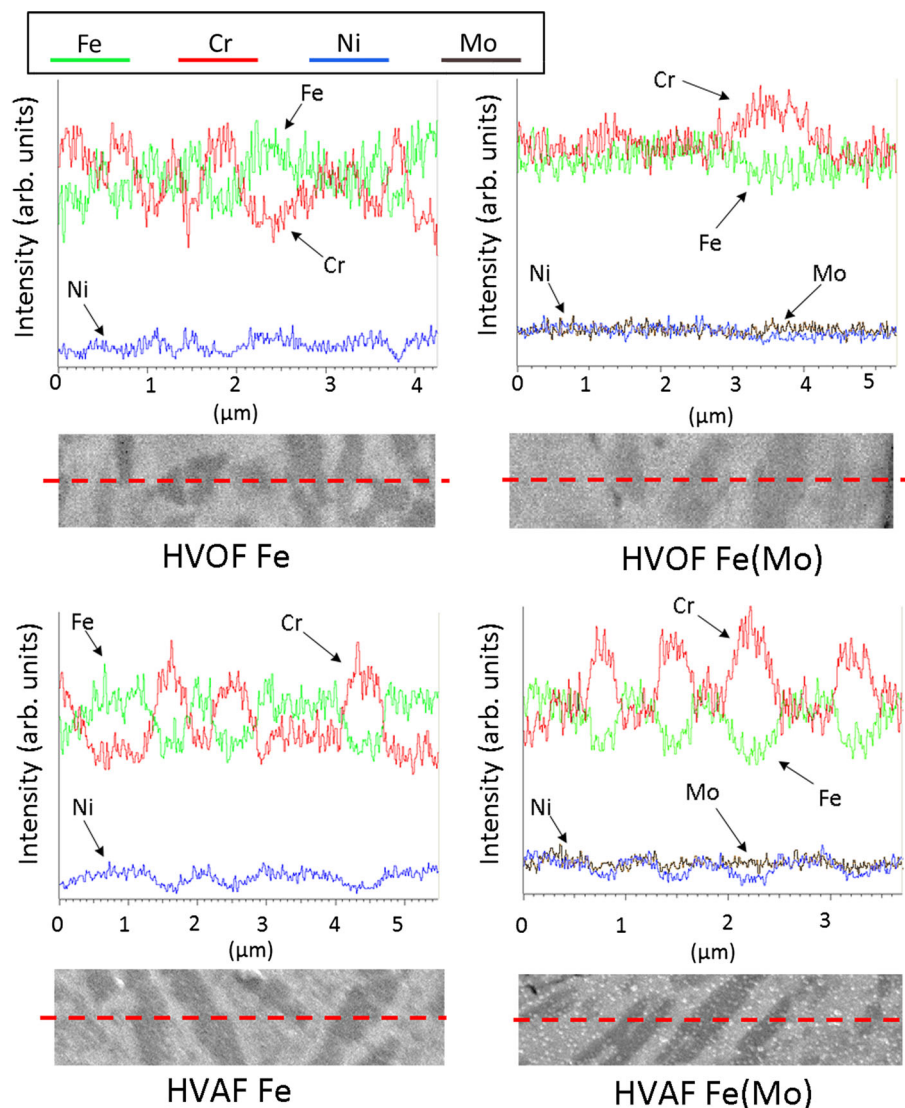


Fig. 8 EDX linescan microanalysis on the corresponding FESEM investigated areas of coatings. Fe, Cr, Ni, and Mo represented in HVOF Fe, HVOF Fe(Mo), HVOF Fe, and HVOF Fe(Mo) coatings

which can be attributed to the glass transition of the residual glassy phase (after the re-crystallization process at 600 °C).

Conversely, HVOF-sprayed coatings retained better the microstructure of the powders and the particles were much likely softened without reaching complete melting; hence, they got flattened upon impact due to the high velocity provided by the HVOF spraying process.

3.3 Micromechanical Properties of Coatings

The micro-hardness of all coatings (Fig. 12, 3 N load) was fairly high (≈ 900 HV_{0.3}) reaching a value up to 950 HV_{0.3} for HVOF Fe. Superior micro-hardness is reported in this study when compared with the Fe-based thermal spray coatings investigated in previous studies (Ref 28, 29, 34). In micro-hardness tests (3 N load, cor-

responding to a maximum penetration depth of ≈ 4000 nm), both intra-lamellar properties and inter-lamellar cohesion are influential (Ref 34-36), due to the discontinuous nature of particle boundaries. It is therefore hypothesized that, compared to previous papers, the higher gas spraying pressures in the present work much likely provided higher particle velocities resulting in a more energetic impact of the particles and, in turn, in a larger intra-lamellar hardness. Moreover, oxide-free particle boundaries were reported in the present study, which results in higher interlocking of particles and in turn, higher mechanical properties.

On the other hand, nano-hardness, due to the low penetration depths (≈ 200 nm at maximum load), primarily reflected the intra-lamellar hardness of single particle material without the effect of particle boundaries (Ref 34, 36).

All studied coatings showed slightly higher intra-lamellar hardness than the powders (Fig. 12). The formation of a supersaturated solid solution (particularly in the case of the HVOF-sprayed coatings, see section 3.2) and grain refinement were thought to be the possible strengthening mechanisms occurring after particle deposition. The increase in nano-hardness after spraying, however, was to be more significant for the Fe(Mo) composition than for the Fe one. HVOF Fe(Mo), in particular, showed the highest intra-lamellar hardness (Fig. 12), which may be due to the fact that this composition is more sensitive to the structural changes described in section 3.2, including the creation of a metastable,

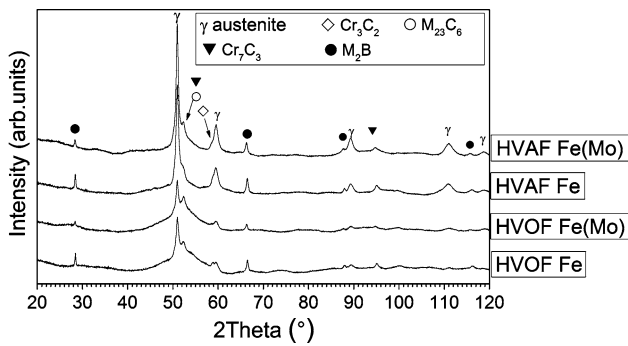


Fig. 9 XRD patterns of coatings, legend: M = Fe, Cr

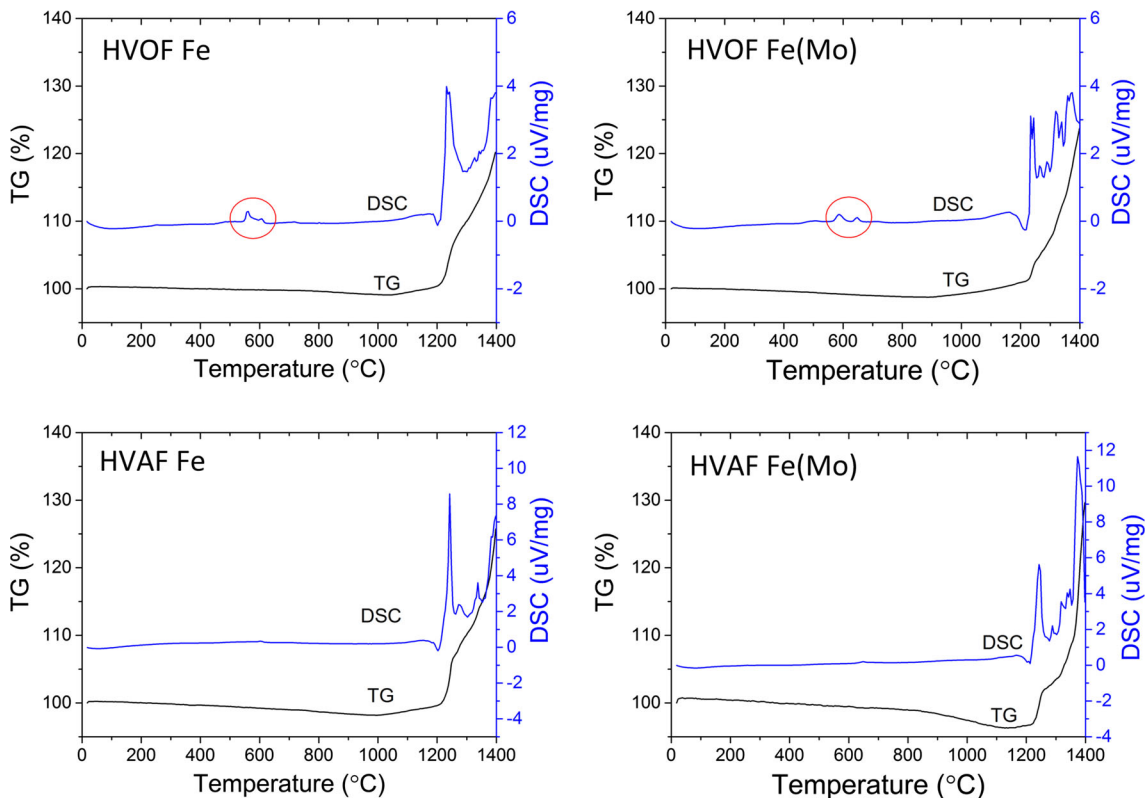


Fig. 10 DSC and TG analyses of the coatings

supersaturated solid solution (especially for the HVOF sample) and the grain refinement (especially for the HVAF one).

Elasticity values ($\eta_{IT} = W_{el}/W_{tot}$) of coatings and single particles are collected in Table 4. Coating surface elasticity is characteristic of the quality of particle boundary. Indeed, in thermal spray coatings the weakest points are particle boundaries which, if defected or oxidized, cannot accommodate shear strain during mechanical testing (Ref 34, 36). As shown in Table 4, the decreased elasticity of coatings when compared to powders is mainly due to particle boundaries, which are discontinuities in the material and inevitably lower the elastic response. However, besides the quality of particle boundaries, the overall elasticity of the coating is also affected by the single splat elasticity. Specifically, HVOF Fe(Mo) has simultaneously the highest coating surface elasticity (good quality of particle boundary) and, together with HVOF Fe, the highest single splat elasticity (elasticity characteristic of material).

Therefore, it is inferred that the modifications occurring during HVOF spraying (including the formation of an amorphous, supersaturated solid solution from melt quenching: see section 3.2) improve the intrinsic elasticity. Furthermore, the HVOF process provides high quality of particle boundaries leading to higher overall coating elasticity.

With regards to HVAF-sprayed coatings, despite the similar single splat elasticity (HVAF Fe = 32.8 ± 5.4 ,

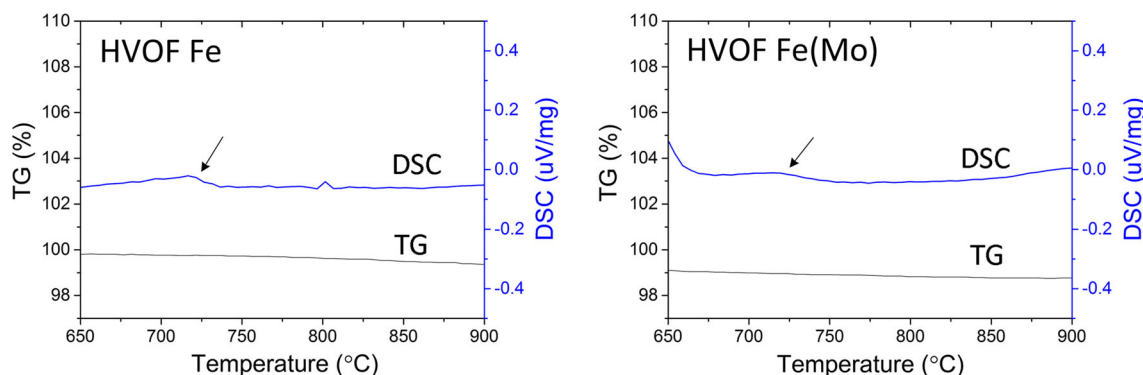


Fig. 11 DSC and TG analysis of HVOF Fe and HVOF Fe(Mo). Small endothermic effect attributed to glass transition

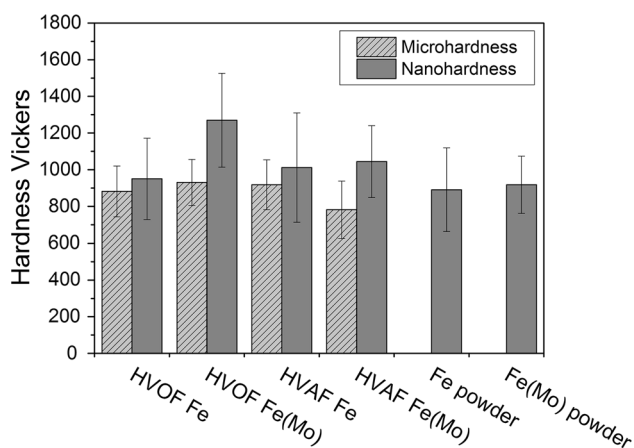


Fig. 12 Micro- and nano-hardness of coatings and nano-hardness of powders

HVAF Fe(Mo) = 32.3 ± 3.7), the difference in coating surface elasticity (HVAF Fe = 21.2 ± 2.1 , HVAF Fe(Mo) = 19.4 ± 2.9) suggested slightly defected particle boundaries of HVAF Fe(Mo). With the purpose of explaining such difference, additional x-ray (Co-K α radiation) residual stress analysis, using the ω -tilt method (Ref 32), was done on polished HVAF-sprayed coatings and the results are shown in Fig. 13 and Table 3. HVAF Fe(Mo) possesses slightly less compressive residual stresses, which might be due to the slightly more defected particle boundaries. It might also explain the lower microhardness of HVAF Fe(Mo). This is also in accordance with the higher affinity of Fe(Mo) (Fig. 5) with oxygen which might have worsened particle bonding, thus lowering the quality of particle boundaries obtained after HVAF spraying. Conversely, when sprayed with HVOF the difference in elasticity and micro-hardness was not perceivable because of the strengthening mechanism which might have hindered any slight difference at particle boundaries. These assumptions need further study related to quantitative analysis of hard precipitates, composition, and crystalline phases.

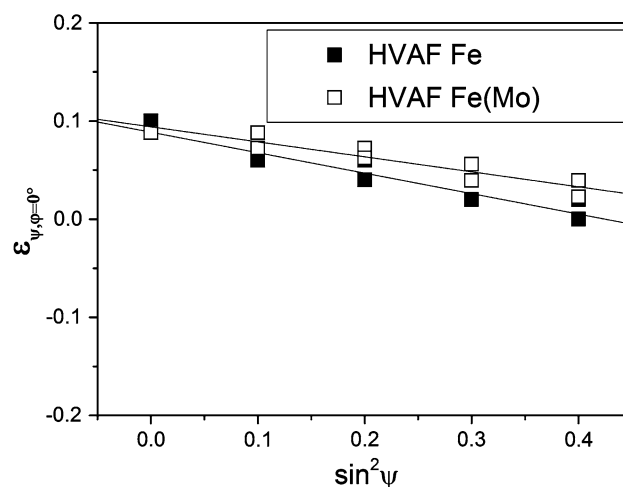


Fig. 13 ε_{ψ} vs. $\sin^2\psi$ plots along direction $\phi = 0^\circ$ calculated on polished coatings of austenite plane ($h k l$) = (3 1 1)

Table 3 Residual stress calculated by XRD analysis

	σ_1 , MPa	σ_2 , MPa	$\sigma_1 + \sigma_2$, MPa	τ_{12} , MPa
HVAF Fe	-273	-287	-560	-28
HVAF Fe(Mo)	-203	-286	-489	-107

Values recalculated with optimized value of d_0 unstressed planar distance of austenite plane ($h k l$) = (3 1 1)

Furthermore, as shown in Fig. 14, no perceivable difference in hardness is seen between the polished and the scratched surface (both when using 10 and 20 N scratching loads), at all indentation loads. This proved the absence of work hardening in all of the studied coatings. It is worth saying that, in a previous work (Ref 37), a similar Fe-based coating showed work-hardening effect during cavitation test due to plastic deformation caused by the bubble collapse and absorption of impact energy. In the light of the considerations made with scratch testing in this paper, the inconsistency of the work-hardening behavior can be

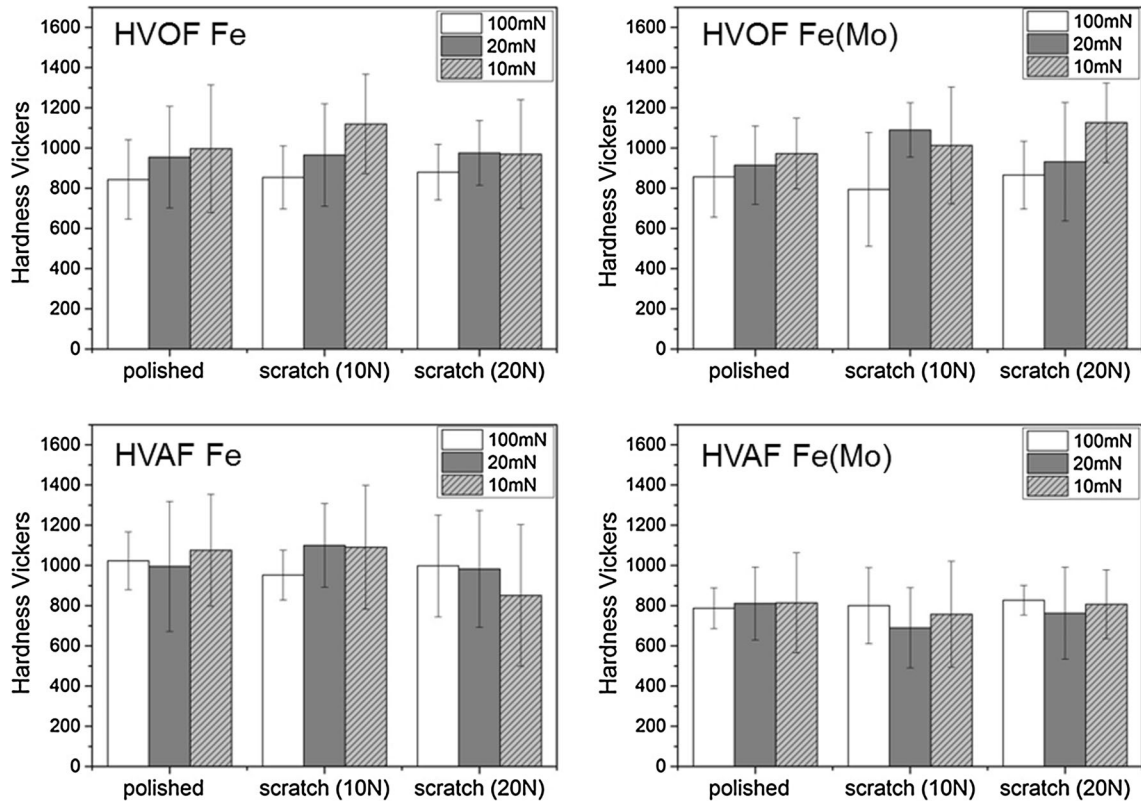


Fig. 14 Nano-hardness performed on scratch (10 and 20 N) and on polished surface at three different indentation loads (10, 20, and 100 mN)

explained as follows: the different loading conditions in the cavitation erosion test (high frequency impacts of micro-jets after bubble implosion in proximity of the coatings surface) led to work hardening. In scratch tests, the much lower loading rates (quasistatic conditions) might have hindered work hardening of the material.

3.4 Wear Behavior of Coatings

Room-temperature sliding wear behavior was investigated using pin-on-disk test with ball-on-disk configuration. In all cases, at the very early stage of the test (<1000 s), the friction coefficient is similar at about 0.5-0.6 (typical of steel-alumina) (Fig. 15). However, after ≈ 1000 s (in the case of Fe(Mo) coatings) or ≈ 2000 -3000 s (in the case of Fe coatings), the friction coefficient rose and stabilized at higher values. Interestingly, such increase of friction coefficient corresponds to a simultaneous decrease of the penetration depth of the ball (Fig. 15). This was probably due to the onset of tribo-oxidation mechanisms, which are clearly seen by SEM observations and EDX analyses of the worn track (Fig. 16). Dark clusters were accordingly seen (Fig. 16, label 1) and their EDX spectra exhibited large peaks of O, Cr, and Fe suggesting mixed oxide formation. The SEM micrographs of the worn track also showed that the clusters consisted of a large number of finely ground debris particles, oxidized and sticking to one another.

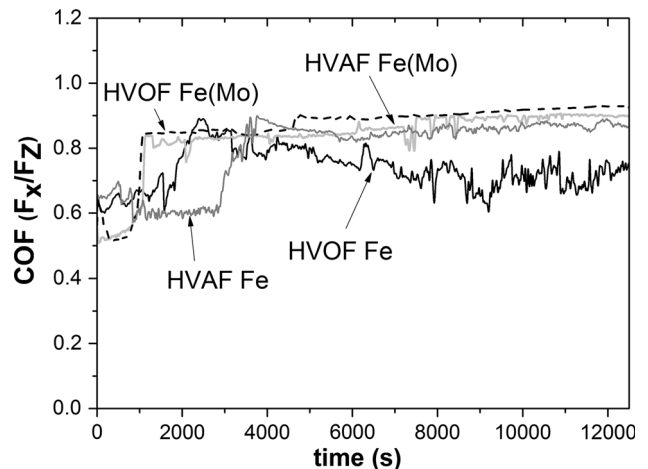


Fig. 15 Friction coefficient recorded for coatings tested against Al_2O_3 ball

Assuming that the increase of friction coefficient is due to the occurrence of tribo-oxidation, the delayed increase of friction in the HVOF Fe samples (Fig. 15) is consistent with the thermal analysis tests made on the powders. Indeed, the Fe(Mo) powder showed an onset of oxidation already at 600 °C (Fig. 5). By contrast, the Fe powder only started to oxidize at higher temperatures, i.e., longer time is needed before flash heating of the wear track and of the

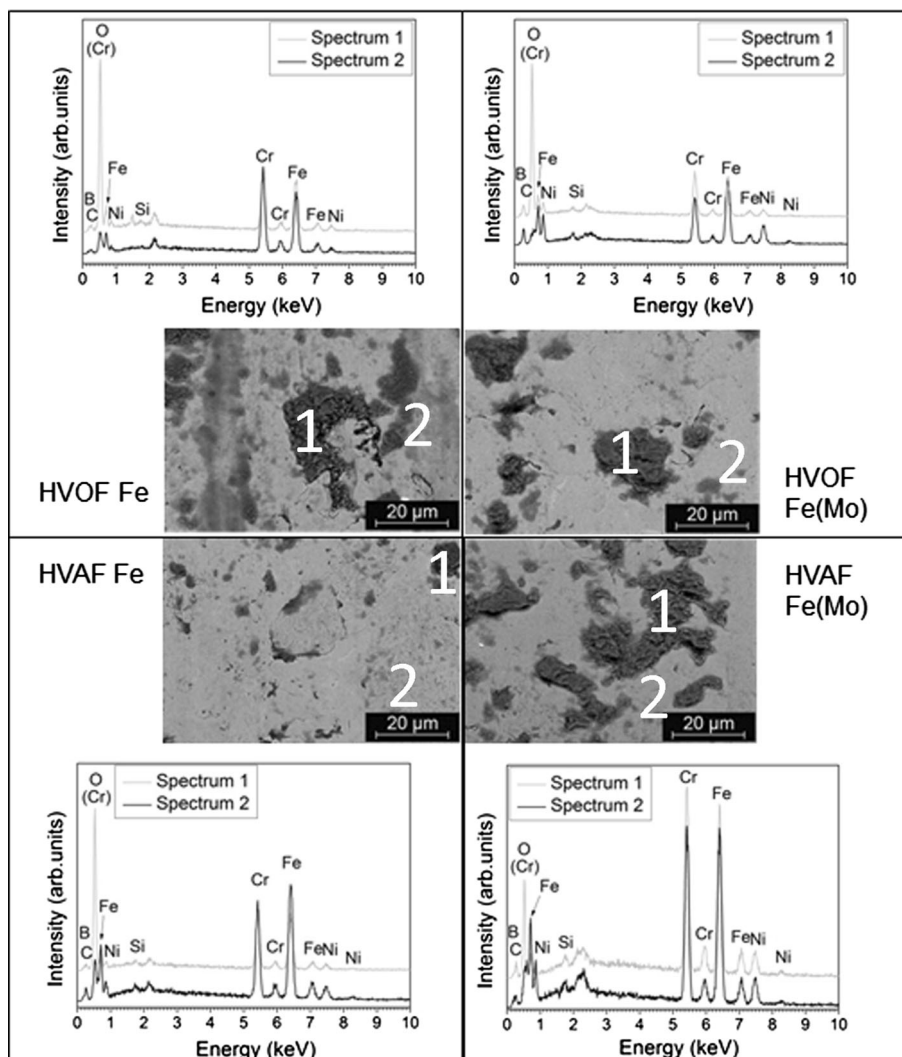


Fig. 16 Back scattered electron SEM micrographs of the wear scars produced after ball-on-disk test and EDX spot analysis

loose debris particles that can trigger oxidation phenomena (Ref 34).

In various cases, the clusters seemed to refill holes formed by particle pull out. Therefore, having said that, a combination of abrasive (small abrasive grooves), delaminative (particle pull out), and tribo-oxidative wear (cluster of tiny oxidized debris into holes formed by particle pull out) was thought to occur for all coatings by observation of SEM micrographs and EDX spot chemical analysis on wear scars (Fig. 16). Additionally, the higher occurrence of delaminative wear in HVOF Fe, causing repeated changes to the superficial conditions in the wear track, might have caused a less stable friction coefficient throughout the test, as seen in the friction curve (Fig. 15) (Ref 28, 38). Delamination may occur because of adhesive wear and related stick-slip phenomena.

It is indeed important to remember that, in metallic thermal spray coatings, one of the most recurring sliding wear mechanisms is adhesive wear due to micro welding of tiny surface asperities between the tested surface and

the counterpart, as explained in Ref 17, 34. This indeed causes severe shear stresses on the particles and lamellae exposed to the outer surface, and particle pull out occurs if the cohesive strength is limited (Ref 17, 34). A similar mechanism was also found by Bolelli et al. (Ref 39), who reported that the noise in the friction curve of a metallic coating might reflect stick-slip phenomena associated with the continuous formation and rupture of surface junctions between the sample and the counterbody, whose surface is covered by a transfer layer of metal from the tested sample. Moreover, abrasive wear is usually present due to the hard asperities of the counterpart, which can plow and cut through the softer metallic sample. Abrasive wear might be also triggered by tiny hard oxide debris particles caught between the counterparts due to tribo-oxidation (Ref 34).

In order to confirm the previous assumption on the wear mechanisms occurring during sliding wear test, cross sections of the worn samples were analyzed by FESEM (Fig. 17). Both HVAF-sprayed samples showed poorly

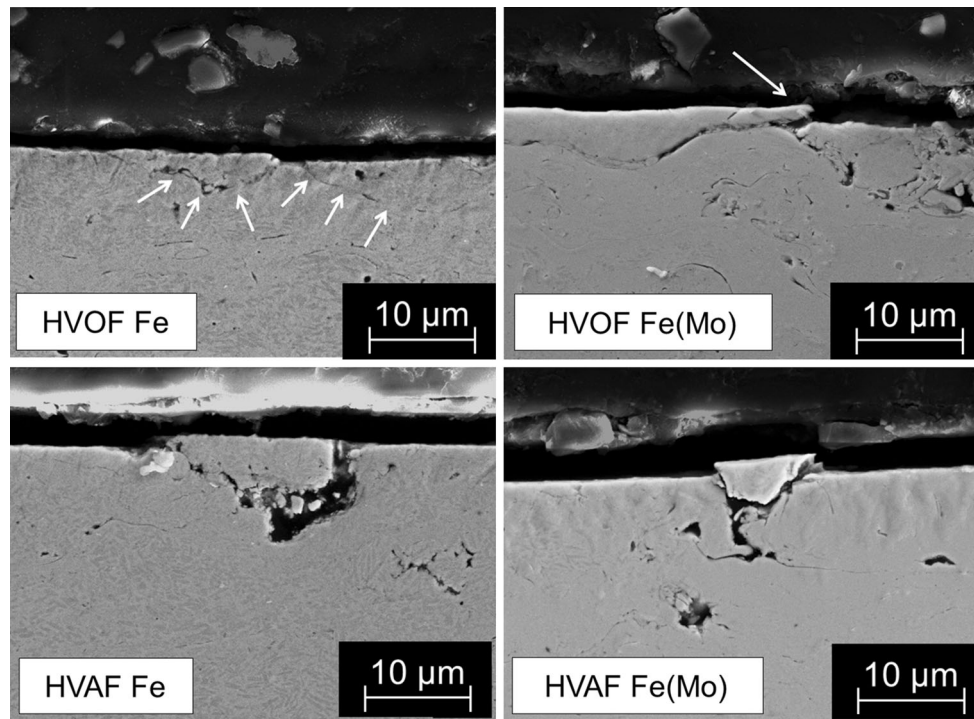


Fig. 17 Cross sections of worn surfaces after sliding wear test. FESEM images

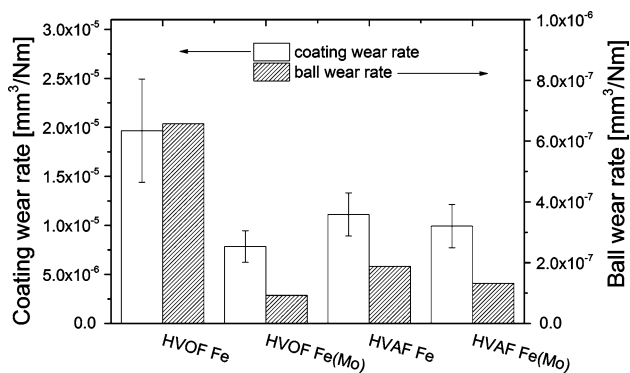


Fig. 18 Wear rates of HVOF and HVOF coatings and alumina counterpart

bonded particles, which were partially pulled out (Fig. 17) probably due to the delaminative wear as previously stated. HVOF Fe showed extensive superficial cracking mainly along the particle boundaries (white arrows Fig. 17), obviously promoting more severe particle pull out. Instead, on HVOF Fe(Mo), which exhibited the lowest wear rate and also produced the lowest counterpart wear (Fig. 18), plastic shearing and extrusion of splats through the deformation of well-bonded superficial lamellae was observed (white arrow Fig. 17). In that case, microcracks did not extend along the whole lamellar boundary. This results in the coating with the lowest

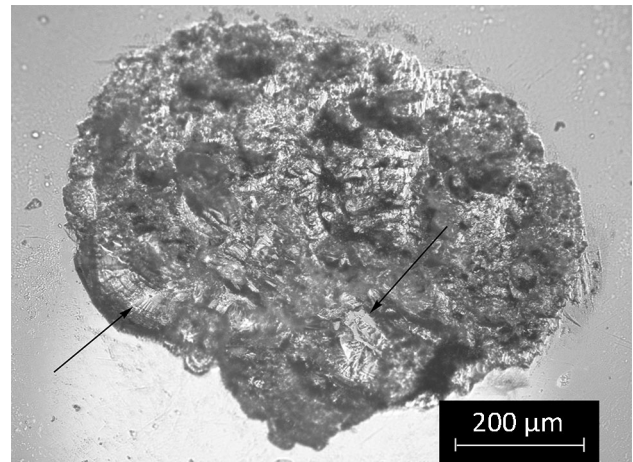


Fig. 19 Wear scar of spherical alumina monocrystalline after sliding against HVOF Fe coating. OM images

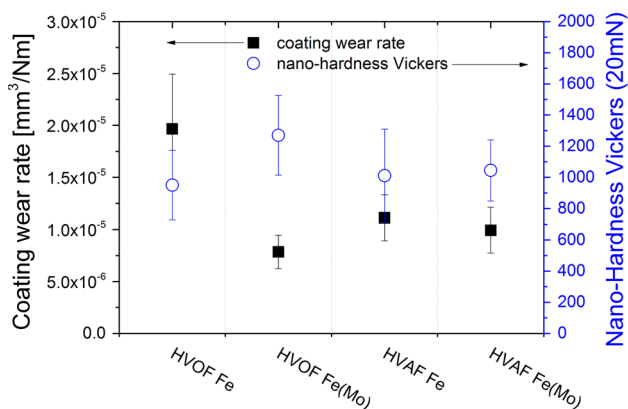
sliding wear rate. A similar behavior has been well described by Edrisy et al. (Ref 17).

The spherical counterparts were also inspected after wear test by optical microscopy, showing similar wear scars for all studied samples. Their wear mechanism was dominated by brittle fracture and fatigue wear inferable by smooth fracture surfaces and fatigue bands, respectively (Fig. 19). The presence of an irregular tribofilm (appearing as dark areas on the worn surface of Fig. 19)

Table 4 Coating surface elasticity and single splat elasticity of coatings

	Coating surface elasticity (η_{rr}), %	Single splat elasticity (η_{rr}), %
HVOF Fe	22.6 ± 2.4	33.7 ± 3.5
HVOF Fe(Mo)	24.1 ± 1.6	35.2 ± 5.2
HVAF Fe	21.2 ± 2.1	32.8 ± 5.4
HVAF Fe(Mo)	19.4 ± 2.9	32.3 ± 3.7
Fe powder	...	37 ± 4.1
Fe(Mo) powder	...	40 ± 5.5

Powders elasticity for comparison

**Fig. 20** Coating wear rate vs. nano-hardness of HVOF and HVAF coatings

corroborates to the previous assumptions on adhesive wear and stick-slip phenomena possibly occurring between the coating and the transferred material on the counterbody surface.

Supposedly, the highest nano-hardness of HVOF Fe(Mo) reduced micro welding, adhesive wear, and abrasive wear. Moreover, HVOF Fe(Mo) was reported to have the highest coating surface elasticity (Table 4) proving good particle boundaries which might further reduce particle pull out. Interestingly, a clear correlation is reported between intra-lamellar hardness and coating sliding wear rate proving the great effect of nano-hardness on diminishing the adhesive wear mechanism in HVOF and HVAF Fe and Fe(Mo) coatings (Fig. 20). With regard to Fe(Mo) powders, HVOF Fe(Mo) and HVAF Fe(Mo) have quite similar friction coefficient (Fig. 15). However, the difference in intra-lamellar hardness and in inter-lamellar cohesion (as proven by the higher overall surface elasticity, section 3.3) led to lower wear rate in the HVOF Fe(Mo) coating. With regards to HVOF Fe, despite the high nano-hardness, delaminative wear together with intrinsic brittleness of such coating might have played a detrimental role in sliding wear promoting brittle fracture and crack propagations (Fig. 17) which in turn lowered the wear resistance (highest wear rate). Conversely, HVAF Fe showed lower wear rate much likely due to the higher micro- and nano-hardness.

4. Conclusions

The present study aimed to acquire a better understanding of the effect of two different thermal spray processes (HVOF and HVAF spraying) on the deposition of two Fe-based powders with Fe-31Cr-12Ni-3.6B-0.6C and Fe-31Cr-12Ni-2Mo-3.6B-0.6C composition (respectively labeled “Fe” and “Fe(Mo)”). The particle surface temperatures were measured by two-color pyrometry technique at the spray distance. Dry sliding wear behavior was studied at room temperature and the wear mechanism was discussed in relation to the microstructural features, mechanical properties, and thermal behavior of the coatings.

– Microstructure

HVOF-sprayed coatings exhibited more microstructural alterations than HVAF-sprayed ones when compared to the corresponding feedstock powders. Precipitate-free particles with high aspect ratio were deposited due to the higher particle temperature during HVOF spraying (≈ 1800 °C), compared to the HVAF process (≈ 1400 °C), which led to carbide/boride dissolution. Additional exothermic peaks in the DSC analysis of the HVOF coatings much likely correspond to carbide/boride re-precipitation. Moreover, small amounts of amorphous phase might have been formed by melt quenching in the HVOF-sprayed coatings, as witnessed by the presence of an inflection in the DSC curves, which is characteristic of the glass transition phenomenon.

– Mechanical properties

All coatings exhibited larger nano-hardness than the corresponding powders. Specifically, the structural and microstructural changes occurring to the HVOF-sprayed Fe(Mo) composition led to high nano-hardness and high surface elasticity at both intra- and inter-lamellar levels. This was also indicative of high inter-lamellar cohesion, thanks to the high-velocity impact of molten or semi-molten droplets and to a proper selection of process parameters, preventing the occurrence of perceivable oxidation phenomena. The low surface elasticity and micro-hardness of HVAF Fe(Mo) was explained to be due to slightly defected particle boundaries as proven by lower compressive residual stress when compared to HVAF Fe. Moreover, nano-indentation tests carried out onto polished and scratched surfaces revealed no evidence of work-hardening behavior in any of the coating samples.

– Dry sliding wear mechanism

The sliding of an Al₂O₃ ball counterpart against the Fe-based coatings at room temperature produced a combination of abrasive, adhesive/delaminative, and tribo-oxidative wear.

Despite the high coefficient of friction, HVOF Fe(Mo) coating exhibited the lowest sliding wear rate accompanied by the lowest counterpart wear. The highest nano-hardness of such coating much likely reduced the abrasive wear by small debris particles and also reduced

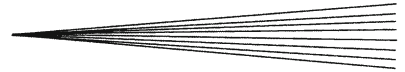
the tendency towards adhesive wear. No work-hardening effect in scratch test can instead be invoked to explain the differences in coating wear rates. Further study of the composition and of the crystalline phase of the oxides formed during sliding wear tests might help towards a further understanding of differences in wear rates and friction coefficients in different wear mechanisms.

Acknowledgments

The authors would like to thank Mr. Mikko Kylmälahti of Tampere University of Technology, Department of Materials Science, for spraying the coatings, M.Sc. Jarmo Laakso, of Tampere University of Technology, Department of Materials Science, for FESEM studies of worn surfaces, and Dr. Paola Miselli, of University of Modena and Reggio Emilia, Department of Engineering “Enzo Ferrari”, for performing the DTA/TG analyses. The study was supported by the Finnish National Graduate School (Concurrent Mechanical Engineering) and Tampere University of Technology.

References

1. P. Martin, *Handbook of Deposition Technologies for Films and Coatings: Science, Applications and Technology*, Elsevier, Oxford, 2009
2. J.R. Davis, Ed., *Surface Engineering for Corrosion and Wear Resistance*, ASM International, Materials Park, 2001
3. L. Pawlowski, *The Science and Engineering of Thermal Spray Coatings*, 2nd ed., Wiley, Chichester, 2008
4. G. Bolelli, L. Lusvarghi, and R. Giovanardi, A Comparison between the Corrosion Resistances of Some HVOF-Sprayed Metal Alloy Coatings, *Surf. Coat. Technol.*, 2008, **202**, p 4793-4809
5. G. Bolelli, L.M. Berger, M. Bonetti, and L. Lusvarghi, Comparative Study of the Dry Sliding Wear Behaviour of HVOF-Sprayed WC-(W, Cr)2C-Ni and WC-CoCr Hardmetal Coatings, *Wear*, 2014, **309**, p 96-111
6. J.M. Miguel, J.M. Guilemany, and S. Vizcaino, Tribological Study of NiCrBSi Coating Obtained by Different Processes, *Tribol. Int.*, 2003, **36**, p 181-187
7. M.R. Ramesh, S. Prakash, S.K. Nath, P. Kumar, and B. Venkataraman, Solid Particle Erosion of HVOF Sprayed WC-Co/NiCrFeSiB Coatings, *Wear*, 2010, **269**, p 197-205
8. F.K. Crundwell, M.S. Moats, V. Ramachandran, T.G. Robinson, and W.G. Davenport, *Extractive Metallurgy of Nickel, Cobalt and Platinum Group Metals*, Elsevier, Amsterdam, 2011
9. D. Beyersmann, Effects of Carcinogenic Metals on Gene Expression, *Toxicol. Lett.*, 2002, **127**, p 63-68
10. A. Arita, M.Y. Shamy, Y. Chervona, H.A. Clancy, H. Sun, M.N. Hall, Q. Qu, M.V. Gamble, and M. Costa, The Effect of Exposure to Carcinogenic Metals on Histone Tail Modifications and Gene Expression in Human Subjects, *J. Trace Elem. Med. Biol.*, 2012, **26**, p 174-178
11. Q. Ke, T.P. Ellen, and M. Costa, Nickel Compounds Induce Histone Ubiquitination by Inhibiting Histone Deubiquitinating Enzyme Activity, *Toxicol. Appl. Pharmacol.*, 2008, **228**, p 190-199
12. L.J. Smith, A.L. Holmes, S.K. Kandpal, M.D. Mason, T. Zheng, and J.P. Wise, The Cytotoxicity and Genotoxicity of Soluble and Particulate Cobalt in Human Lung Fibroblast Cells, *Toxicol. Appl. Pharmacol.*, 2014, **278**, p 259-265
13. H. Hériaud-Kraemer, G. Montavon, S. Hertert, H. Robin, and C. Coddet, Harmful Risks for Workers in Thermal Spraying: A Review Completed by a Survey in a French Company, *J. Therm. Spray Technol.*, 2003, **12**, p 542-554
14. L.-M. Berger, Hardmetals as Thermal Spray Coatings, *Powder Metall.*, 2007, **50**, p 205-214
15. M.F. Morks, Y. Tsunekawa, and M. Okumiya, Characterization and Properties of Splats Sprayed with Different Cast Iron Powders, *Mater. Lett.*, 2004, **58**, p 2481-2485
16. K. Volenik, F. Hanousek, P. Chráska, J. Ilavský, and K. Neufuss, In-Flight Oxidation of High-Alloy Steels During Plasma Spraying, *Mater. Sci. Eng. A*, 1999, **272**, p 199-206
17. A. Edrissy, T. Perry, Y. Cheng, and A. Alpas, Wear of Thermal Spray Deposited Low Carbon Steel Coatings on Aluminum Alloys, *Wear*, 2001, **251**, p 1023-1033
18. O. Redjidal, B. Zaid, M.S. Tabti, K. Henda, and P.C. Lacaze, Characterization of Thermal Flame Sprayed Coatings Prepared from FeCr Mechanically Milled Powder, *J. Mater. Process. Technol.*, 2013, **213**, p 779-790
19. B. Wielage, H. Pokhmurska, M. Student, V. Gvozdeckii, T. Stupnyckij, and V. Pokhmurskii, Iron-Based Coatings Arc-Sprayed with Cored Wires for Applications at Elevated Temperatures, *Surf. Coat. Technol.*, 2013, **220**, p 27-35
20. B. Fu, D. He, and L. Zhao, Effect of Heat Treatment on the Microstructure and Mechanical Properties of Fe-Based Amorphous Coatings, *J. Alloys Compd.*, 2009, **480**, p 422-427
21. G. Bolelli, I. Hulka, H. Koivuluoto, L. Lusvarghi, A. Milanti, K. Niemi, and P. Vuoristo, Properties of WC-FeCrAl Coatings Manufactured by Different High Velocity Thermal Spray Processes, *Surf. Coat. Technol.*, 2014, **247**, p 74-89
22. R.Q. Guo, C. Zhang, Q. Chen, Y. Yang, N. Li, and L. Liu, Study of Structure and Corrosion Resistance of Fe-Based Amorphous Coatings Prepared by HVOF and HVOF, *Corros. Sci.*, 2011, **53**, p 2351-2356
23. G. Bolelli, T. Börner, A. Milanti, L. Lusvarghi, J. Laurila, H. Koivuluoto, K. Niemi, and P. Vuoristo, Tribological behavior of HVOF- and HVOF-Sprayed Composite Coatings Based on Fe-Alloy + WC-12% Co, *Surf. Coat. Technol.*, 2014, **248**, p 104-112
24. R.Q. Guo, C. Zhang, Y. Yang, Y. Peng, and L. Liu, Corrosion and Wear Resistance of a Fe-Based Amorphous Coating in Underground Environment, *Intermetallics*, 2012, **30**, p 94-99
25. L. Liu and C. Zhang, Fe-Based Amorphous Coatings: Structures and Properties, *Thin Solid Films*, 2014, **561**, p 70-86
26. A. Verstab and V. Baranovski, *Deposition of Carbides*, Activated Combustion HVOF Spraying, Virginia, 2004
27. S. Kuroda, M. Watanabe, K. Kim, and H. Katanoda, Current Status and Future Prospects of Warm Spray Technology, *J. Therm. Spray Technol.*, 2011, **20**, p 653-676
28. A. Milanti, H. Koivuluoto, P. Vuoristo, G. Bolelli, F. Bozza, and L. Lusvarghi, Microstructural Characteristics and Tribological Behavior of HVOF-Sprayed Novel Fe-Based Alloy Coatings, *Coatings*, 2014, **4**, p 98-120
29. A. Milanti, H. Koivuluoto, and P. Vuoristo, Influence of the Spray Gun Type on Microstructure and Properties of HVOF-Sprayed Fe-Based Novel Corrosion Resistant Coatings, *Thermal Spray 2014: Not Fiction: Thermal Spray the Key Technology in Modern Life!*, 2014, Barcelona, Spain, 2014
30. J.F. Archard, Contact and Rubbing of Flat Surfaces, *J. Appl. Phys.*, 1953, **24**, p 981-988
31. ISO, *Metallic Materials, Instrumented Indentation Test for Hardness and Materials Parameters*, ISO 14577-1:2002(E), ISO, Geneva, 2002
32. A. Milanti, V. Matikainen, H. Koivuluoto, G. Bolelli, L. Lusvarghi, and P. Vuoristo, Effect of Spraying Parameters On The Microstructural and Corrosion Properties of HVOF-Sprayed Fe-Cr-Ni-B-C Coatings, *Surf. Coat. Technol.*, 2015, **277**, p 81-90
33. A. Edrissy, A.T. Alpas, T. Perry, Wear Mechanism Maps for Thermal-Spray Steel Coatings, *Metall. Mater. Trans. A*, 2005, **36**, p 2737-2750
34. G. Bolelli, B. Bonferroni, J. Laurila, L. Lusvarghi, A. Milanti, K. Niemi, and P. Vuoristo, Micromechanical Properties and Sliding Wear Behaviour of HVOF-Sprayed Fe-Based Alloy Coatings, *Wear*, 2012, **276-277**, p 29-47
35. G. Bolelli, L.-M. Berger, T. Börner, H. Koivuluoto, L. Lusvarghi, C. Lyphout, N. Markocsan, V. Matikainen, P. Nylén,



- P. Sassatelli, R. Trache et al., Tribology of HVOF- and HVAF-sprayed WC-10Co4Cr Hardmetal Coatings: A Comparative Assessment, *Surf. Coat. Technol.*, 2015, **265**, p 125-144
36. J. Nohava, B. Bonferroni, G. Bolelli, and L. Lusvarghi, Interesting Aspects of Indentation and Scratch Methods for Characterization of Thermally-Sprayed Coatings, *Surf. Coat. Technol.*, 2010, **205**, p 1127-1131
37. A. Milanti, H. Koivuluoto, P. Vuoristo, G. Bolelli, F. Bozza, and L. Lusvarghi, Wear and Corrosion Resistance of High-Velocity Oxygen-Fuel Sprayed Iron-Based Composite Coatings, *Proceedings of the ASME 2013 International Mechanical Engineering Congress and Exposition, Emerging Technologies*, Vol. 11, V011T06A01, San Diego, CA, 2013
38. C.W. Park, M.W. Shin, and H. Jang, Friction-Induced Stick-Slip Intensified by Corrosion of Gray Iron Brake Disc, *Wear*, 2014, **309**, p 89-95
39. G. Bolelli, A. Candeli, L. Lusvarghi, A. Ravoux, K. Cazes, A. Denoirjean, S. Valette, C. Chazelas, E. Meillot, and L. Bianchi, Tribology of NiCrAlY + Al₂O₃ Composite Coatings by Plasma Spraying with Hybrid Feeding of Dry Powder + Suspension, *Wear*, 2015, **344-345**, p 69-85